

# Recent advances in $\beta$ -FeSe $_{1-x}$ and related superconductors

Maw-Kuen Wu<sup>1,2</sup>, Ming-Jye Wang<sup>2,3</sup> and Kuo-Wei Yeh<sup>2</sup>

<sup>1</sup> Department of Physics, National Dong-Hwa University, Hualien, Taiwan

<sup>2</sup> Institute of Physics, Academia Sinica, Taipei, Taiwan

<sup>3</sup> Institute of Astronomy and Astrophysics, Academia Sinica, Taipei, Taiwan

E-mail: [mkwu@phys.sinica.edu.tw](mailto:mkwu@phys.sinica.edu.tw)

Received 15 October 2012

Accepted for publication 20 November 2012

Published 21 February 2013

Online at [stacks.iop.org/STAM/14/014402](http://stacks.iop.org/STAM/14/014402)

## Abstract

It has been more than four years since the discovery of  $\beta$ -FeSe $_{1-x}$  superconductors. Through the efforts of many outstanding research groups, unprecedented advances in the field have been achieved. High-quality single crystals of  $\beta$ -FeSe $_{1-x}$  and related compounds have been prepared by various techniques, allowing us to explore in detail the physical properties of this class of materials. Detailed characterizations of the structure and properties of these crystals have helped us to understand the origin of superconductivity in  $\beta$ -FeSe $_{1-x}$ . The occurrence of superconductivity is associated with the low-temperature structure distortion, which is accompanied by several anomalies. Recent measurements on quasiparticle and acoustic phonon dynamics with respect to the orbital modification in  $\beta$ -FeSe $_{1-x}$  suggest the opening of an energy gap below 130–140 K, accompanied by a coincident transfer of optical spectral weight in the visible range and alterations in transport properties. These observations provide convincing evidence that the modification of the electronic structure occurs prior to the lattice distortion. They further suggest that the high-temperature gap and the lattice symmetry breaking are driven by short-range orbital and/or charge orders.


Keywords: FeSe, superconductors, high-quality single crystals, structure and properties characterization

## 1. Introduction

The discovery of superconductivity with a critical temperature  $T_c \sim 10$  K in  $\beta$ -FeSe $_{1-x}$  (hereafter referred to as 11 system) [1] has attracted much attention because of having the simplest crystal structure (figure 1) among Fe-based superconductors and relatively high  $T_c$  (up to 37 K) under pressure [2]. A subsequent chemical doping study showed that  $T_c$  could be enhanced by partial substitution of Se by Te [3]. More interestingly, the crystal symmetry of  $\beta$ -FeSe $_{1-x}$  was observed to undergo a distortion at about 100–105 K into a monoclinic structure (space group  $P112/n$ , or orthorhombic with the defined  $ab$  plane rotated by

$\sim 45^\circ$  with respect to the original lattice) [4, 5]. Thus a detailed characterization of the electronic and magnetic behavior and their interplay with structural peculiarities may contribute to a more fundamental understanding of this class of materials. Recently, a new bilayer compound,  $A_x\text{Fe}_2\text{Se}_2$  (where A stands for alkaline metal) [6] was found to be a superconductor with  $T_c > 30$  K. This new development has generated extensive research of this class of material. Furthermore, intercalation of alkaline-metal-based liquid ammonia in the FeSe bilayer has resulted in the observation of superconductivity with a substantially enhanced  $T_c$ . An extremely large superconducting-like gap was observed by both scanning tunneling microscopy and angle-resolved photoemission spectroscopy on monolayer  $\beta$ -FeSe $_{1-x}$  prepared by molecular beam epitaxy (MBE).

Immediately after the discovery of 11 systems, extensive investigations to better understand this material have

 Content from this work may be used under the terms of the [Creative Commons Attribution-NonCommercial-ShareAlike 3.0 licence](http://creativecommons.org/licenses/by-nc-sa/3.0/). Any further distribution of this work must maintain attribution to the author(s) and the title of the work, journal citation and DOI.

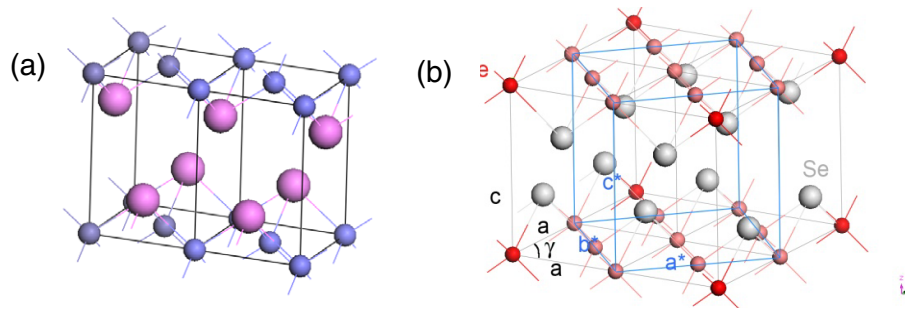


**Figure 1.** (a) Crystal structure of tetragonal FeSe showing Fe in blue and Se in purple. (b) The structure (plotted in gray lines) is transformed to a monoclinic (space group  $P112/n$ ) lattice with a  $\gamma$  angle larger than  $90^\circ$  at low temperatures. The distorted lattice may also be considered as orthorhombic with the defined  $ab$  plane rotated by  $45^\circ$  with respect to the original lattice (blue lines).

been carried out. Several groups have optimized the preparation of polycrystalline samples and measurement of the chemical stoichiometry of the 11 compounds. Unfortunately, controversy remains as to whether they are Fe rich or Se deficient. Efforts were spent on the preparation of superconducting thin films [4]. It was found that relatively high quality thin films could be prepared by laser ablation. An interesting orientation and thickness dependence of the superconductivity was observed in the pristine 11 and Te-doped 11 compounds [7, 8].

In polycrystalline samples, the existence of second phases at the grain boundaries complicates the correlation of structure with electronic properties, including the superconducting properties. Bulk samples prepared by high-temperature solid-state synthesis normally consist of a major tetragonal phase and minor phases such as ferrimagnetic hexagonal  $\delta$ -FeSe, ferromagnetic hexagonal  $\text{Fe}_7\text{Se}_8$ , monoclinic  $\text{Fe}_3\text{Se}_4$ ,  $\text{Fe}_3\text{O}_4$  and pure Fe. Single crystals are crucial for studying the correct phase devoid of impurities and for better understanding the underlying mechanisms. Therefore, many groups initiated the crystal growth soon after the discovery of superconductivity in  $\beta$ -FeSe $_{1-x}$ .

This review summarizes our research activities on  $\beta$ -FeSe $_{1-x}$  and related compounds in the past few years. We begin with the methods developed to grow single crystals and textured thin films. Then we present our understanding of the material properties in both the normal state and superconducting state. Finally, we summarize our current understating of the correlation between the observed properties and the occurrence of superconductivity.

## 2. Crystal growth

### 2.1. $\beta$ -FeSe $_{1-x}$ crystal growth

Bulk samples prepared by high-temperature solid-state synthesis typically contain impurities, including ferrimagnetic hexagonal  $\delta$ -FeSe, ferromagnetic hexagonal  $\text{Fe}_7\text{Se}_8$ , monoclinic  $\text{Fe}_3\text{Se}_4$ ,  $\text{Fe}_3\text{O}_4$  and pure Fe. This problem may be overcome by the use of high-quality single crystals whose chemical composition and crystal structure can be properly determined. As single crystals are important for obtaining the correct phase devoid of impurity phases, many groups initiated the crystal growth soon after the discovery

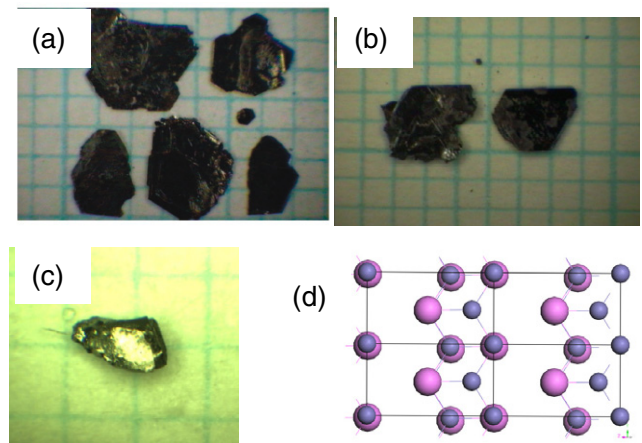


**Figure 2.** A photograph (background mesh size 1 mm) of  $\text{FeSe}_{0.88}$  crystals grown by the flux method [4]; (b)  $\beta$ -FeSe $_{1-x}$  crystals grown by CVT; (c)  $\text{Fe}_{1.01}\text{Se}$  crystal grown by high-pressure cubic anvil technique. The front surface of these crystals is perpendicular to the crystal (101) axis. (d) The atomic configuration of  $\beta$ -FeSe $_{1-x}$  (101) crystal plane. Fe is shown in blue and Se in purple.

of superconductivity in  $\beta$ -FeSe $_{1-x}$ . From the reported phase diagram  $\beta$ -FeSe $_{1-x}$  is known to melt congruently around  $1075^\circ\text{C}$  [9]. However, considerable difficulties arise when growing crystals of  $\beta$ -FeSe $_{1-x}$  by the melt growth techniques because of the high viscosity of the melt and the high vapor pressure of Se at this temperature. Therefore, crystals were grown by low-temperature methods, such as molten salt flux growth and vapor transport growth. Zhang *et al* [10] grew FeSe $_x$  crystals by the flux method using NaCl/KCl as a flux. Rectangular and hexagonal crystals with dimensions of several hundreds of microns have been grown using  $\text{FeSe}_{0.82}$  powder with NaCl/KCl in a 1 : 1 ratio as the starting materials. They contained  $\beta$ -FeSe $_{1-x}$  but with a high volume of intergrown  $\delta$ -FeSe. The as-grown crystals show a superconductivity onset at 11.9 K with zero resistance ( $T_{c,0}$ ) at 3.4 K. Mok *et al* [5] grew  $\text{FeSe}_{0.88}$  crystals from KCl solutions. Large hexagonal plates of  $\sim 2$ – $3$  mm width and 0.1–0.3 mm thickness are shown in figure 2(a). The crystal plate surface is identified to be the (101) face of  $\beta$ -FeSe $_{1-x}$ . The crystals contained the  $\beta$ -FeSe $_{1-x}$  phase with minor amounts of hexagonal FeSe and showed a resistive transition width of  $\sim 3.5$  K. The flux-grown crystals typically suffer from flux contamination and water-induced degradation of

the sample during the separation from the flux. The crystals are normally stacked with pieces of small grains and therefore show a large in-plane imperfection, despite having a highly oriented (101) out-of-plane crystallinity.

Vapor transport is a superior method for the preparation of bulk single crystals with low twin and dislocation densities. Patel *et al* [11] used a physical vapor transport (PVT) approach to grow  $\beta$ -FeSe $_{1-x}$  crystals with lateral dimensions ranging from a few hundred micrometers to 1–2 mm. Although they predominantly contained the  $\beta$ -phase, trace amounts of  $\delta$ -phase were also detected. Crystals of  $\beta$ -FeSe $_{1-x}$  were grown by vapor transport with I $_2$  as a carrier gas [12]. The growth was carried out in a 200–250 mm long quartz ampoule with a temperature gradient from 700 °C at the hot end to 300 °C at the cold end. The growing time was relatively long, 2–4 weeks. The crystals obtained were typically around 1 mm $^2$  in size, and their composition depended on position in the ampoule.

We found that  $\beta$ -FeSe $_{1-x}$  crystals grown by CVT with I $_2$  as a gas carrier deteriorated soon after exposure to air, probably due to the I $_2$  contamination on the surface of the crystals. Therefore, we tried to use iron(III) bromine (FeBr $_3$ ) as the carrier to grow  $\beta$ -FeSe $_{1-x}$  crystals. Thermodynamic arguments suggest the following growth mechanism: FeBr $_3$  thermally dissociates at above 400 °C producing Br $_2$  vapor, which then reacts with FeSe positioned in the hotter zone to form FeBr $_3$  and Se vapors. These vapors diffuse from the hotter source zone to the cooler growth zone where their reaction reversely produces solid FeSe and gaseous FeBr $_3$ . The charge held at 800 °C with the growth zone at 700 °C and a temperature gradient along the tube of about 6 °C cm $^{-1}$  are optimal for the crystallization. The crystals obtained appear black with mirror-like luster and a typical size of 2 × 2 × 0.05 mm $^{-3}$  as shown in figure 2(b). Their powder x-ray diffraction (XRD) pattern is consistent with a single-phase tetragonal structure. The samples reveal no trace amount of hexagonal phase. XRD on oriented crystals shows reflections from the (101) family of  $\beta$ -FeSe $_{1-x}$ . The superconducting transition width is about 4 K, which may be attributed to the unavoidable non-uniformity of Fe/Se or to slight oxidation.

The cubic-anvil high-pressure technique, which has been utilized for the growth of SmFeAsO $_{1-x}$ F $_y$  [13], MgB $_2$  [14] and CoP $_3$  [15], was also applied to the growth of  $\beta$ -FeSe $_{1-x}$  crystals. The advantage of this technique is that the extremely high pressure can effectively suppress the evaporation of volatile components in the material, which is melted at high temperatures. One of the problems with crystal growth under high-temperature and high-pressure conditions is that the density of the nucleus is high and it is difficult to control nucleation; this hinders growth of large crystals because of the relatively small space for the growth of individual grains. The precursor mixture of stoichiometric compositions was placed in a boron nitride crucible and heated, forming the melt at a pressure of 10 kbar and temperatures of 1000–1050 °C. The difficulty in controlling nucleation in the high-pressure technique is reflected in the quality of crystals grown—many have irregular shapes and form clusters of several crystals. Plate-like crystals consist of a high volume fraction of superconducting  $\beta$ -FeSe $_{1-x}$ ; on the other hand, crystals with

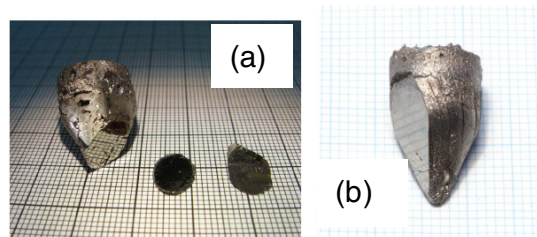


**Figure 3.** Single-crystal boules of FeSe $_{0.3}$ Te $_{0.7}$  on a 1 mm grid grown by the (a) Bridgman method [17] (the two dark objects are crystals grown by the flux method) (reprinted with permission from [17], copyright 2009 by The American Physical Society) and (b) optical zone-melting technique [21]. The lustrous surface of the boule is perpendicular to the crystal  $c$ -axis.

long columnar shape are non-superconducting hexagonal FeSe. As shown in figure 2(c), single crystals of  $\beta$ -FeSe $_{1-x}$  can be separated and the crystals can reach a size of up to 1 × 1 mm $^2$ .

$\beta$ -FeSe $_{1-x}$  crystals grown by one of the techniques mentioned above always exhibit an inevitable intergrowth of  $\delta$ -FeSe and a nonuniform compositional distribution, and therefore have a wide superconducting transition. Annealing at 400 °C *in situ* during the cooling appears to be beneficial to the properties of the crystals [4, 16]. However, it is still a mystery why the  $\beta$ -FeSe $_{1-x}$  crystals were grown to have the plate-like habit of a (101) facet with the atomic arrangement shown in figure 2(d). These binary  $\beta$ -FeSe $_{1-x}$  crystals cannot be cleaved in any condition, yet the important feature of in-plane crystallinity that may affect the interpretation of anisotropic properties was not fully discussed.

## 2.2. FeSe $_{1-x}$ Te $_x$ crystal growth

It is difficult to obtain large single crystals of superconducting  $\beta$ -FeSe $_{1-x}$  phase using the growth techniques mentioned above. Therefore, the isostructural Fe–Te–Se system which crystallizes relatively easy and has a higher  $T_c$  than that of Fe–Se is much more promising for the successful growth of single crystals. FeSe $_{1-x}$ Te $_x$  crystals can be easily grown from the high-temperature melt using the Bridgman method [17–20]. The elements were sealed in a double quartz crucible, melted together at a temperature above 1000 °C, and then cooled in a temperature gradient at rates ranging from 3 to 6 °C h $^{-1}$  to a temperature between 350 and 750 °C, followed by furnace cooling. Large crystals can be separated, especially in the composition of FeSe $_{0.3}$ Te $_{0.7}$ , as shown in figure 3(a). FeSe $_{1-x}$ Te $_x$  single crystals can also be grown by the optical zone-melting technique proposed by Yeh *et al*. The samples were zone-melted using a focused halogen light source and moved at a rate of 1–2 mm h $^{-1}$  to control the crystallization rate [21]. As shown in figure 3(b), a crystal of excellent quality grew perpendicular to the  $c$ -axis along the direction of ampoule translation, indicating a well-controlled growth.

Considerable difficulties occur when growing crystals of low Te concentrations ( $x < 0.3$ ), and only crystals with  $x > 0.3$  can be obtained. Resistivity measurements show superconductivity for crystals of  $x = 0.4–0.9$  (figure 4(a))

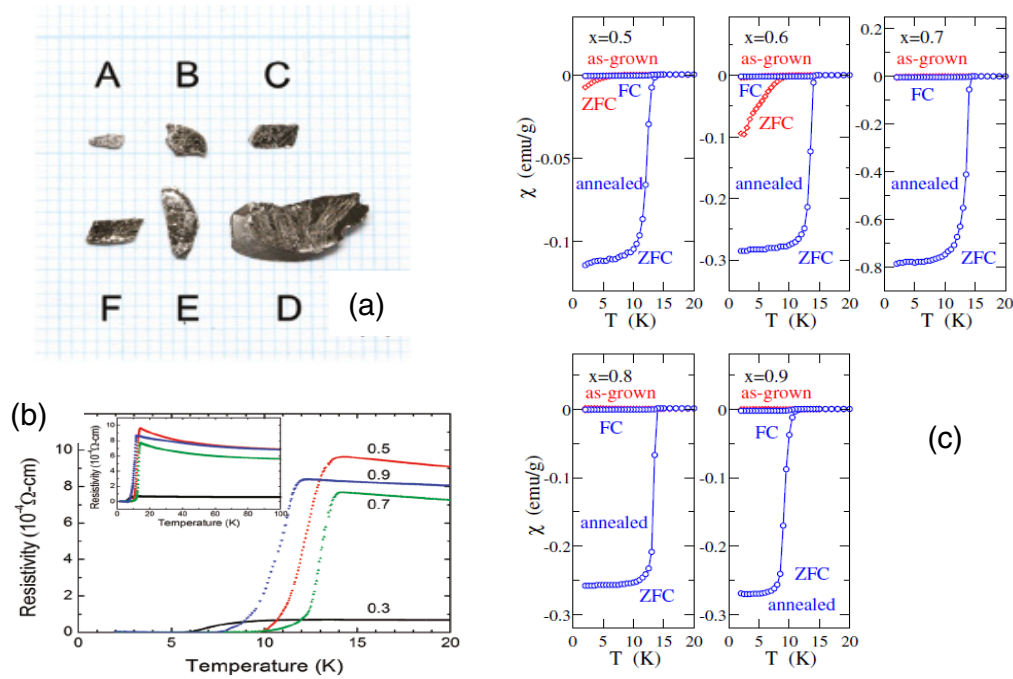


**Figure 4.** (a)  $\text{FeSe}_x\text{Te}_{1-x}$  crystals with  $x = 0.3, 0.5, 0.6, 0.7, 0.9$  and  $1.0$  (A–F, respectively). (b) Temperature dependences of the in-plane resistivity for  $\text{FeSe}_{1-x}\text{Te}_x$  crystals ( $0.3 < x < 0.9$ ) at temperatures  $0$ – $20$  K [21]. The inset shows the in-plane resistivity in the range  $0$ – $100$  K. (c) Magnetic susceptibility, in a magnetic field of  $1$  mT parallel to the  $c$ -axis on zero-field cooling (ZFC) and field cooling (FC) for as-grown and annealed single crystals of  $\text{FeSe}_{1-x}\text{Te}_x$  with  $x = 0.5$ – $0.9$  [19].

with maximum onset transition temperatures around  $14$  K for  $x = 0.5$ – $0.7$ , as shown in figure 4(b). It was noted that most of the as-grown crystals exhibited non-uniform distribution of Se and Te. Post annealing at temperatures above  $700^\circ\text{C}$  would homogenize the Se/Te distribution [21]. A recent work revealed that, as shown in figure 4(c), single crystals of  $x = 0.5$ – $0.9$  annealed at  $400^\circ\text{C}$  for at least  $100$  h in vacuum exhibit bulk superconductivity [19]. The  $\text{FeSe}_{1-x}\text{Te}_x$  crystals are comparably large and of better quality than FeSe crystals. Importantly, these crystals can be cleaved in ultrahigh vacuum for surface-sensitive spectroscopic experiments.

### 2.3. Growth of doped FeSeTe crystals

The FeSe system demonstrates the interplay of structure, magnetism and superconductivity. Chemical substitutions at different atomic sites have a significant effect on the emergence or suppression of superconductivity. Recently, Wu *et al* [4] reported the substitution effect of different metals, such as Al, Ti, V, Cr, Mn, Co, Ni, Cu, Ga, In, Ba and Sm in superconducting  $\beta$ -FeSe $_{1-x}$ . All of the transition metals (Ti, V, Cr, Mn, Co, Ni and Cu) were incorporated into the FeSe structure with a substitution ratio below  $10$  at.%. It was claimed that Fe ions can be substituted by Co up to  $50$  at.% [22], and disappearance of superconductivity was reported for all  $\beta$ -FeSe $_{1-x}$  samples substituted by Co at above  $2.5$  at.% [21]. In contrast, for Fe $_{1-z}$ Co $_z$ Se $_{1-x}$  with  $z$  equal to  $0.05$  and  $0.1$ , the critical onset temperature ( $T_{c,\text{onset}}$ ) was  $10$  and  $5$  K, respectively [23]. Zhang *et al* [24] reported the absence of superconducting transition above  $2$  K in Fe $_{0.96}$ Ni $_{0.04}$ Se $_{1-x}$ . However,

Mizuguchi *et al* [23] estimated  $T_{c,\text{onset}}$  at  $10$  K in Fe $_{0.95}$ Ni $_{0.05}$ Se $_{1-x}$ . The solubility limit of Cu in the FeSe $_{1-x}$  phase reached the range of  $20$ – $30$  at.% [25]. It is concluded from these studies that only Fe $_{1-x}$ Cu $_x$ Se $_{1-x}$  samples with  $x < 0.02$  exhibit superconductivity while those with  $x > 0.03$  are semiconductors [4, 25, 26]. It is noteworthy that superconductivity of  $\beta$ -FeSe $_{1-x}$  where Fe was substituted by Co, Ni and Cu was strongly suppressed; however, Mn substitution up to  $30$  at.% only slightly changed the  $T_c$  value [26] and increased the  $T_c$  at a low doping level of  $2$  at.% [27].

Most of the samples with various elements substituting Fe in both systems of  $\beta$ -FeSe $_{1-x}$  and FeTe $_{1-x}$ Se $_x$  have been prepared by a conventional solid-state reaction. Although FeSe is chemically amenable to a wide variety of substitutions, the growth of sizable high-quality crystals remains a challenge. Thus, a high-quality FeSe $_{0.5}$ Te $_{0.5}$  crystal, which had a higher  $T_c$ , was studied to address the substitution effect on superconductivity. Fe $_{0.9}$ TM $_{0.1}$ Se $_{0.5}$ Te $_{0.5}$  crystals, where TM is transition metal, are prone to exfoliation and readily cleave from an ingot because of the layered crystal structure. Shiny  $c$ -axis-oriented crystals with dimensions up to  $5 \times 2$  mm $^2$  can be easily cleaved, as shown in figures 5(a) and (b). In contrast to polycrystalline samples, these crystals consist of a single chemical phase. As seen in figure 5(c), dopant concentrations in these crystals are close to the nominal values.

As shown in figure 6(a), cobalt substitution results in monotonous structural contractions along the  $a$ - and  $c$ -axis. Clearly, the lattice contraction for Fe $_{1-x}$ Co $_x$ Se $_{0.5}$ Te $_{0.5}$  crystals is much larger than those of Fe $_{1-x}$ Co $_x$ Se $_{0.85}$  [22, 23] and

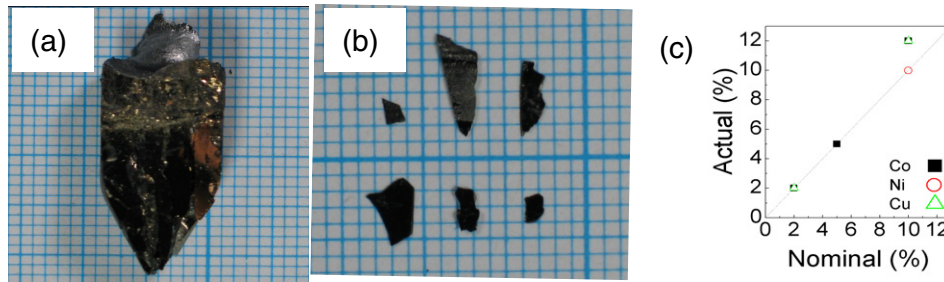


**Figure 5.** (a) As-grown  $\text{Fe}_{0.9}\text{Cu}_{0.1}\text{Se}_{0.5}\text{Te}_{0.5}$  crystal on a 1 mm grid. The lustrous surface is perpendicular to crystal  $c$ -axis. (b) The upper three crystals represent  $\text{Fe}_{0.9}\text{TM}_{0.1}\text{Se}_{0.5}\text{Te}_{0.5}$  crystals with  $\text{TM} = \text{Fe}, \text{Ni}$  and  $\text{Cu}$ , from left to right, respectively. The lower three crystals from left to right are  $\text{Fe}_{1-x}\text{Co}_x\text{Se}_{0.5}\text{Te}_{0.5}$  ( $x = 0.02, 0.05$  and  $0.1$ , respectively). (c) The linear correlation between the nominal and measured crystal compositions.

$\text{Fe}_{1-x}\text{Co}_x\text{Se}_{0.5}\text{Te}_{0.5}$  bulk samples [24, 28, 29]. This can be explained by the fact that the Co substitution levels on Fe sites in polycrystalline samples are overestimated due to a possible segregation in the grain boundaries and impurity phases. The structural variations of  $\text{Fe}_{1-x}\text{Cu}_x\text{Se}_{0.5}\text{Te}_{0.5}$  samples reveal that lattice constants decrease as iron is replaced by copper, in agreement with the dependence of polycrystalline  $\text{Fe}_{1-x}\text{Cu}_x\text{Se}_{0.5}\text{Te}_{0.5}$  samples [28]. However, it remains unclear why the lattice parameter  $a$  increases with Cu substitution for polycrystalline  $\text{Fe}_{1.01-x}\text{Cu}_x\text{Se}$  samples [25]. The lattice contractions of 0.3% along the  $a$ -axis and 0.6% along the  $c$ -axis are much smaller than 0.9% (both for the  $a$ - and  $c$ -axis) of Co-doped  $\text{FeSe}_{0.5}\text{Te}_{0.5}$  crystals, indicating a good correlation with the difference in ionic radii between  $\text{Co}^{2+}$  and  $\text{Cu}^{2+}$ . Figure 6(c) shows resistivity as a function of temperature for  $\text{Fe}_{1-x}\text{Co}_x\text{Se}_{0.5}\text{Te}_{0.5}$  compounds. Small amounts of Co enhance the resistivity and the  $T_{c,\text{onset}}$  decreases from 14 K for  $x = 0$  to 10.2 K for  $x = 0.02$  and 4 K for  $x = 0.05$ . For  $x = 0.1$ , the compound becomes weakly metallic and is not superconducting. Figure 6(d) demonstrates that Cu substitution suppresses the superconductivity. A resistivity drop is observed at  $T_{c,\text{onset}} = 5.6$  K and the resistivity does not reach zero for  $x = 0.02$ ; moreover,  $\text{Fe}_{0.9}\text{Cu}_{0.1}\text{Se}_{0.5}\text{Te}_{0.5}$  crystals show Mott insulating phases common for polycrystalline [26] and single-crystalline samples [30]. The superconductivity was destroyed by as little as 2% Cu substitution.

The reason for the easy suppression of superconductivity in  $\beta\text{-FeSe}_{1-x}$  remained unresolved, whether it is a result of structural disorder induced by substitution or whether the unpaired 3d electrons play a crucial role in generating competition between magnetic and superconducting phases. Rietveld refinements of the powder diffraction data at room temperature are summarized to give insight into the substitution effect on crystal structure. The angle of the Se–Fe–Se bond across the Fe-plane and the normalized  $T_c$  decrease simultaneously by TM substitution. The overall effects of the doping are compressing the  $\text{FeSe}_4$  tetrahedra and decreasing the cross-Fe-plane bond angle. The Se–Fe–Se bond angle is reduced more significantly and the superconductivity is suppressed more rapidly for  $\text{Fe}_{1-x}\text{Cu}_x\text{Se}_{0.5}\text{Te}_{0.5}$  than for cobalt-doped  $\text{FeSe}_{0.5}\text{Te}_{0.5}$  crystals. It is noteworthy that in the superconducting  $\beta\text{-FeSe}_{1-x}$  [1],  $\text{FeSe}_{1-x}\text{Te}_x$  [2] and  $\text{Fe}_{1-x}\text{Cu}_x\text{Se}_{0.85}$  [26]

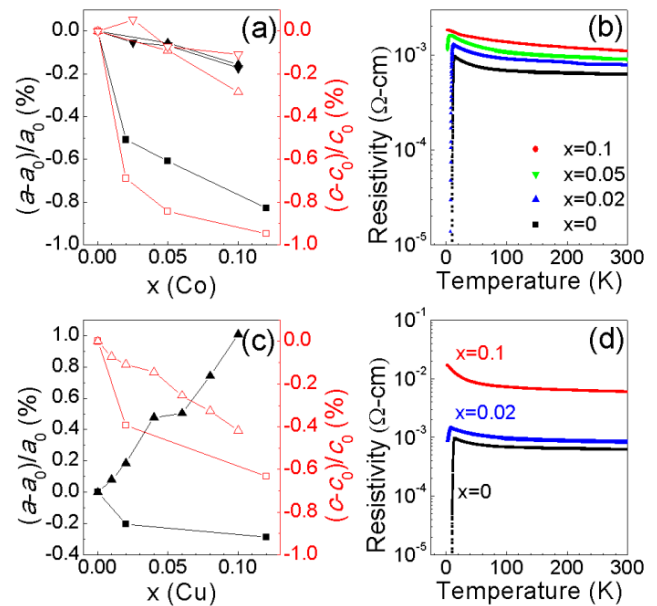


**Figure 6.** (a) Compositional dependence of lattice contraction along the  $a$ -axis (black solid symbols) and  $c$ -axis (red open symbols) for  $\text{Fe}_{1-x}\text{Co}_x\text{Se}_{0.5}\text{Te}_{0.5}$  crystals (squares) and  $\text{Fe}_{1-x}\text{Co}_x\text{Se}$  polycrystalline samples (normal triangles [23] and inverted triangles [22]). (b) Temperature dependence of in-plane resistivity for  $\text{Fe}_{1-x}\text{Co}_x\text{Se}_{0.5}\text{Te}_{0.5}$  crystals ( $x = 0-0.1$ ). (c) Compositional dependence of lattice expansion along the  $a$ -axis (black solid symbols) and  $c$ -axis (red open symbols) for  $\text{Fe}_{1-x}\text{Cu}_x\text{Se}_{0.5}\text{Te}_{0.5}$  crystals (squares) and  $\text{Fe}_{1.01-x}\text{Cu}_x\text{Se}$  polycrystalline samples (triangles) [3]. (d) Temperature dependence of in-plane resistivity for  $\text{Fe}_{1-x}\text{Cu}_x\text{Se}_{0.5}\text{Te}_{0.5}$  crystals ( $x = 0-0.1$ ).

samples, the low-temperature structural distortion occurs at around 100 K signifying a symmetry lowering from the high-temperature tetragonal phase to monoclinic phase ( $P112/n$ ), and this distortion is believed to correlate with the occurrence of superconductivity. We conclude that the TM substitution results in the compression of the  $\text{FeSe}_4$  tetrahedron, which inhibits the structural transition and superconductivity at low temperatures.

#### 2.4. $K_x\text{Fe}_2\text{Se}_2$ crystal growth

The anion height, i.e., the distance between the chalcogen atoms and the Fe plane inside  $[\text{Fe}_2\text{Ch}_2]$  blocks, is an

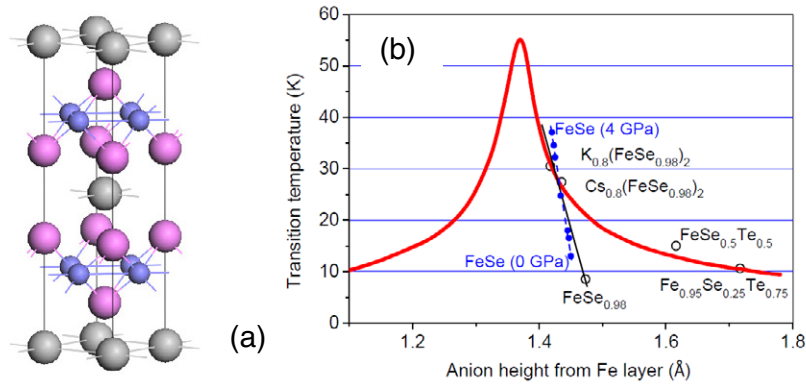


**Figure 7.** (a) Crystal structure of  $K_x\text{Fe}_2\text{Se}_2$  where Fe, Se and K atoms are shown in blue, purple and gray, respectively. The symmetry belongs to the  $I4/mmm$  group with Fe–Se layers separated by K atoms. (b) Dependence of  $T_c$  on the distance between Fe ions and the chalcogenide/pnictide layers [32]. The red line shows the dependence as presented by Mizuguchi *et al* [34] for typical Fe-based superconductors. The solid circles indicate the data obtained for FeSe under high pressure [36]. The open circles indicate the data taken from reports [37, 38].

important parameter affecting the  $T_c$  of Fe-chalcogenides. It can be changed by altering the relative ratios of Se and Te anions or by applying pressure.  $T_{c,\text{onset}}$  increases from 8 K at the ambient pressure to 37 K under 4.5 GPa in FeSe. Intercalation of alkaline metal ions, such as  $\text{K}^+$  [6],  $\text{Rb}^+$  [31] and  $\text{Cs}^+$  [32] into the center of  $\text{Fe}_2\text{Se}_2$  blocks has been reported recently. As a result, the transition temperature was enhanced to above 30 K, and this is so far the highest  $T_c$  among the Fe chalcogenides under ambient pressure. This superconductivity is associated with a structural change from 11-type ( $P4/nmm$ ) to 122-type ( $I4/mmm$ ). Figure 7(a) shows the crystal structure of  $K_x\text{Fe}_2\text{Se}_2$ . The Fe–Fe layer distance is 7.0184 Å in comparison with 2.7617 Å in  $\beta\text{-FeSe}_{1-x}$  [33]. The intercalation of K also increases the Fe–Se bond length within the layers by 2.15%.

The enhanced superconductivity of this novel phase may be related to structural characteristics, such as the anion height and Se–Fe–Se bond angles. These values for  $K_x\text{Fe}_2\text{Se}_2$  seem to be closer to the ‘optimum’ values ( $\sim 1.38$  Å and  $109.47^\circ$ ) for iron-based superconductors, as shown in figure 7(b) [34]. The other key factor responsible for the superconductivity in  $K_x\text{Fe}_2\text{Se}_2$  is deficiency of alkaline metal ions, which determines the electron concentration in the systems and for the type of band filling, i.e. the hole doping effect.

To prepare  $K_x\text{Fe}_2\text{Se}_2$  the FeSe precursor and K metal with a nominal ratio of  $\text{K}:\text{FeSe} = 0.8:2$  were placed in a quartz crucible, or in an alumina crucible to prevent reaction with K. The inner crucible was sealed into an outer quartz tube or in an arc-welded stainless-steel tube. The mixture was heated to above  $1000^\circ\text{C}$ , kept at this temperature for at least 2 h, and slowly cooled down to  $750\text{--}800^\circ\text{C}$  at a rate of  $3\text{--}6^\circ\text{C h}^{-1}$  to enable the crystal growth.  $K_x\text{Fe}_2\text{Se}_2$  crystals are easy to cleave, and crystals with a thickness below  $100\ \mu\text{m}$  can be easily obtained, whereas  $\text{Cs}_x\text{Fe}_2\text{Se}_2$  crystals are fragile and difficult to cleave.

$T_{c,\text{onset}}$  is 31 K and 30 K for  $\text{K}_{0.86}\text{Fe}_2\text{Se}_{1.82}$  and  $\text{Cs}_{0.86}\text{Fe}_{1.66}\text{Se}_2$  single crystals, respectively, indicating that the superconducting fraction can be close to 100% for both types of crystals if the preparation is optimized.

The  $H_{c2}$  and the normal-state resistivity are larger than in other iron-based superconductors [35]. The anisotropy  $H_{ab,c2}(0)/H_{c,c2}(0)$  is  $\sim 3$  for both materials. Despite a higher  $T_c$  compared to  $\beta\text{-FeSe}_{1-x}$ , the superconducting transition temperature monotonously decreases with applied pressure, and the material becomes a non-superconducting metal at pressures above  $\sim 9$  GPa [39].

### 3. Preparation of $\text{FeSe}_{1-x}\text{Te}_x$ thin films

$\text{FeSe}_{1-x}\text{Te}_x$  (FST) thin films can be prepared by many methods, such as pulsed laser deposition (PLD) [4, 40–42], molecular beam epitaxy (MBE) [43, 44] and metalorganic chemical vapor deposition (MOCVD) [45]. Various substrates are used for growing epitaxial FST thin films, including  $\text{SrTiO}_3$ , MgO,  $\text{YAlO}_3$ ,  $\text{LaAlO}_3$  (LAO), Si, GaAs and  $\text{r-Al}_2\text{O}_3$ , despite some of them having a large lattice mismatch with  $\text{FeSe}_{1-x}\text{Te}_x$ .  $\text{FeSe}_{1-x}\text{Te}_x$  films are typically grown in a vacuum of  $10^{-5}\text{--}10^{-6}$  Torr to prevent oxidation during deposition. The growth temperature of  $\text{FeSe}_{1-x}\text{Te}_x$  films ranges from 250 to  $600^\circ\text{C}$ .

Most reported epitaxial  $\text{FeSe}_{1-x}\text{Te}_x$  films had their  $c$ -axis preferentially oriented along the out-of-plane direction of the substrate. Wang *et al* [7] have prepared epitaxial FeSe films with (101) preferred orientation on MgO substrate at high temperatures ( $\sim 500^\circ\text{C}$ ). High-resolution transmission electron microscopy (HRTEM) images revealed a thin transition layer ( $\sim 5$  nm) at the interface in (101) preferred orientation films, but not in (001) films. For Te-substituted films, the growth orientation remained along the (001) direction even at high substrate temperatures. In contrast, Huang *et al* [8] demonstrated an in-plane orientation change in  $\text{FeSe}_{0.5}\text{Te}_{0.5}$  films on MgO. The  $a$ -axis of  $\text{FeSe}_{0.5}\text{Te}_{0.5}$  films grown at  $280^\circ\text{C}$  is rotated  $45^\circ$  with respect to the (100) direction of MgO, but it is aligned to the (100) direction when the substrate temperature is increased to  $500^\circ\text{C}$ .

A broadening of XRD peaks was observed in Te-substituted  $\text{FeSe}_{1-x}\text{Te}_x$  films, indicating a phase separation which is common to the bulk [4]. In addition, the

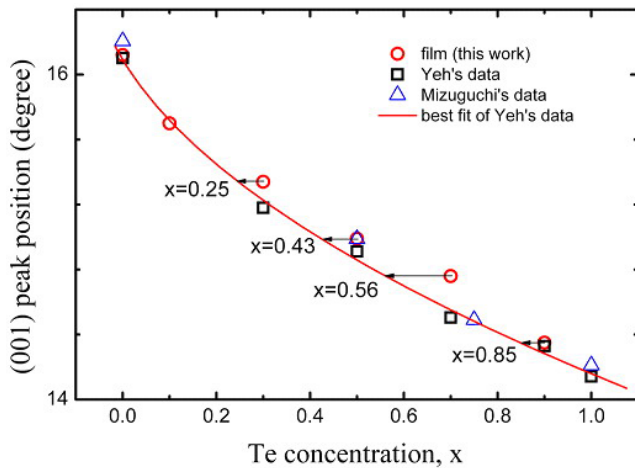


**Figure 8.** The (0 0 1) peak position in  $\text{FeSe}_{1-x}\text{Te}_x$  films as a function of Te concentration. The solid line is the best fit to the data from Yeh *et al* [21]. The corrected Te concentrations of films are marked in the plot.

Se/Te ratio is higher in the film than in the target for PLD. The deviation of Se/Te is attributed to the high vapor pressure of Se. Figure 8 compares the (001) XRD peak position between thin film and bulk samples. The maximum deviation is observed around Se/Te = 1. The actual Se/Te ratios of thin films can be calibrated according to the bulk data.

#### 4. Superconductivity of $\text{FeSe}_{1-x}\text{Te}_x$ films

The substrate may generate compressive or tensile stress in the film grown on it. Usually such stress is uniaxial, which is different from hydrostatic pressure. Additional information on the film state can be extracted through studying the properties of the film. In  $\text{FeSe}_{1-x}\text{Te}_x$  films, many important phenomena related to the superconducting transition were observed, which may clarify the mechanism of superconductivity in Fe-chalcogenides. Several important observations are included below.

Wu *et al* [4] reported a strong suppression of superconductivity in Te-substituted thin films prepared at low temperatures,  $\text{FeSe}_{0.5}\text{Te}_{0.5}$  films, with (001) preferred orientation. However, such suppression is not observed in FeSe films grown with (101) orientation [7]. Further investigations by low-temperature XRD correlated the superconductivity of FeSe film with the structural distortion at low temperatures. Figure 9 shows the temperature evolution of XRD peaks of FeSe films grown at 500 °C (a) and 320 °C (b, c). The FeSe film in figure 9(a) has  $T_c \sim 9$  K. Its (220) XRD peak gradually splits into two peaks upon cooling to temperatures below 80 K, indicating a structural distortion from tetragonal to orthorhombic symmetry. In contrast, the 140-nm-thick FeSe film in figure 9(b) is grown at 320 °C and has  $T_c < 2$  K. Its (221) peak does not split even at 6.5 K. If the thickness of FeSe film grown at 320 °C is increased to 1  $\mu\text{m}$ ,  $T_c$  recovers to about 6 K and the (221) peak broadens below 80 K, as shown in figure 9(c), indicating that the low-temperature structural distortion occurred in part of the thin film.

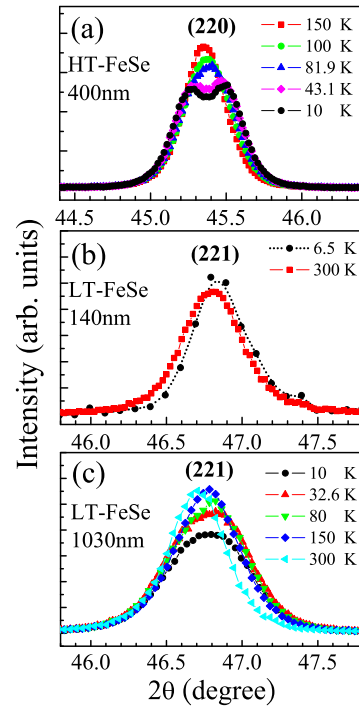


**Figure 9.** (a) XRD (220) peak of a FeSe film grown at 500 °C and measured at different temperatures. The splitting of the Bragg peak indicates a structural distortion at  $\sim 80$  K. XRD (221) peak of (b) 140 nm and (c) 1030 nm thick FeSe films grown at 320 °C and measured at different temperatures. The peak broadens upon cooling for the 1030 nm, but not the 140 nm film.

Huang *et al* [8] reported the suppression of superconductivity in  $\text{FeSe}_{0.5}\text{Te}_{0.5}$  films. The  $a/c$  lattice constant ratio varied linearly with growth temperature, but the unit cell volume remained nearly constant. From the x-ray refinement results, the (Se,Te)–Fe–(Se,Te) bond angle,  $\alpha$ , remained roughly unchanged at about 98° while the  $T_c$  varied greatly. Therefore, Huang *et al* concluded that  $\alpha$  does not significantly affect  $T_c$ ; instead, the position of chalcogen might play an important role. In contrast, Bellingeri *et al* [46] reported an enhanced  $T_c$  up to 21 K in  $\text{FeSe}_{0.5}\text{Te}_{0.5}$  films on LAO substrate. They found that in film with the maximum  $T_c$  of 21 K,  $\alpha$  approaches 109.47°, corresponding to a regular tetrahedron, which is similar to the observation in Fe-pnictide superconductors. More interestingly, FeTe films on MgO substrate can show a superconducting transition around 13 K under tensile stress [47]. As expected, the structural and magnetic first-order transition are softening in superconducting FeTe films. The authors found the Te–Fe–Te bond angle of superconducting films ( $T_c = 7$  K) is larger by 0.75° compared to the non-superconducting films.

#### 5. Characterization

The  $\beta$ - $\text{FeSe}_{1-x}$  crystals were investigated for their microstructure using HRTEM, powder XRD and Raman spectroscopy. Here we briefly present the HRTEM results. To prevent oxidation during TEM sample preparation, the  $\beta$ - $\text{FeSe}_{1-x}$  crystals were crushed, ground, and suspended in two-tree drops of  $n$ -hexane in an argon-filled glove box.

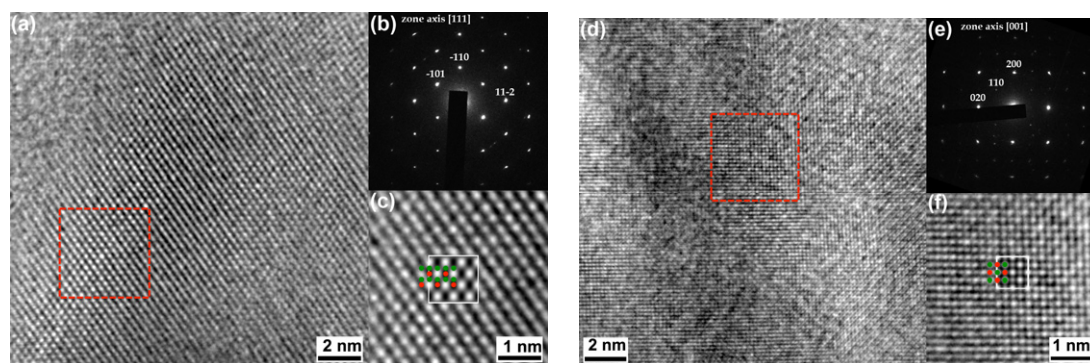


**Figure 10.** (a, d) HRTEM images of  $\text{FeSe}_{0.95}$  crystals viewed along the (111) and (001) crystal orientations, respectively; (b, e) selected area electron diffraction patterns of the same crystals; (c, f) magnified views of the areas marked by dotted squares in (a, d) respectively. A Wiener filter was used to reduce the noise in the experimental images. Insets in (c) and (f) show computer-simulated images for a crystal thickness of 35.3 and 35.3 nm and an objective defocus of 15 and 18 nm, respectively. Green atoms represent Fe and red atoms represent Se.

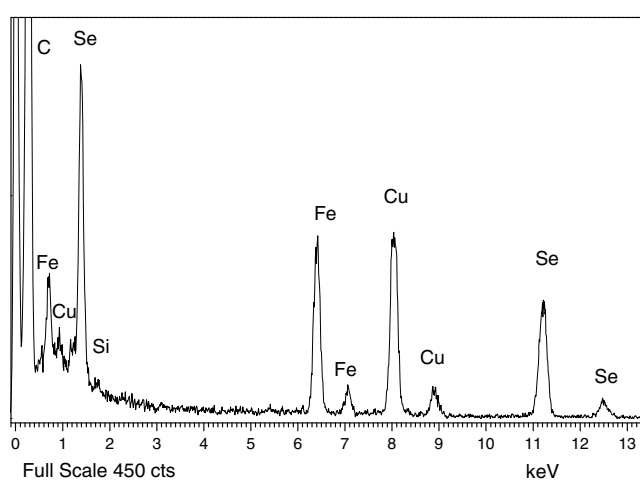


**Figure 11.** EDS analysis of the area shown in figure 10(d), revealing strong Fe and Se peaks. The Cu and C peaks originate from the supporting Cu grid and Lacey film, respectively. Semi-quantitative analysis yields a chemical composition of  $\text{FeSe}_{0.94 \pm 0.04}$ .

### 5.1. HRTEM

The quality of the crystals was assessed by HRTEM (figure 10). The composition of the crystals was nearly the same as the starting composition of the powders, as assessed by energy-dispersive x-ray spectroscopy (EDS, figure 11). Efforts to measure the composition using inductively coupled plasma techniques were not satisfactory as Se reacted with the solvents and formed volatile complexes.

Figures 10(a) and (d) show two HRTEM images of  $\text{FeSe}_{0.95}$  crystal, viewed from the [111] and [001] crystallographic orientations, respectively. Even though the as-grown crystals exhibit a (101) plate habit, there seems to be a natural (100) cleavage, which is seen when crushing the crystal or cleaving it in vacuum for x-ray absorption spectroscopy studies [11, 12]. The powder XRD patterns also show a strong (100) reflection which is not seen in crystal plates. It is therefore not surprising that we see (100) oriented plates in the TEM samples. The extended lattice fringes signify good crystallinity. A 10- $\mu\text{m}$  field-limiting aperture was used (producing a round area of  $\sim 150$  nm diameter) to

create corresponding electron diffraction images. The lattice constants obtained from the diffraction patterns are  $a = b = 3.681 \pm 0.003$  Å and  $c = 5.488 \pm 0.013$  Å, very close to those in the JCPDS card. Figures 10(c) and (f) show, respectively, the magnified images of figures 10(a) and (d), where the experimental noise is reduced by a Wiener filter and the random background is partly subtracted. The individual Fe and Se atoms are hardly resolved in figure 10(c) due to the resolution limit of our TEM. However, when viewed along the  $c$ -axis, the atoms in the  $ab$  plane are resolved, as shown in figure 10(f). Since HRTEM images (phase-contrast images) vary strongly with the sample thickness and the defocus value of the objective lens, it is instructive to compare them with images simulated by established atomic models. Using the thickness, which was estimated from the electron energy loss spectrum (not shown here), and computer-optimized objective defocus value, we simulated HRTEM images for the [111] and [001] crystal orientations. The best matches between experimental and simulated images are shown in the insets of figures 10(c) and (f).

EDS spectra of  $\text{FeSe}_{0.95}$  crystals (figure 11) are dominated by iron and selenium, with other signals originating from the supporting copper grid and Lacey film. Semi-quantitative chemical analysis yielded a composition of  $\text{FeSe}_{0.94 \pm 0.04}$ , in agreement with the nominal composition of the powders used for crystal growth. Similar results were also obtained for a  $\text{FeSe}_{0.85}$  crystal.

### 5.2. Transport properties

The resistivity-temperature curve for single-crystal FeSe (figure 12) is similar to those of polycrystalline samples, suggesting an isotropic system. A more detailed analysis reveals several interesting features, such as an anomaly with onset at about 100 K that corresponds to the structural transition temperature ( $T_s$ , right inset of figure 12). This result further confirms the presence of the low-temperature structural distortion. The second feature is a small resistivity drop at about 40 K, which may be associated with the 40 K superconducting phase observed in  $\beta\text{-FeSe}_{1-x}$  under high pressures.



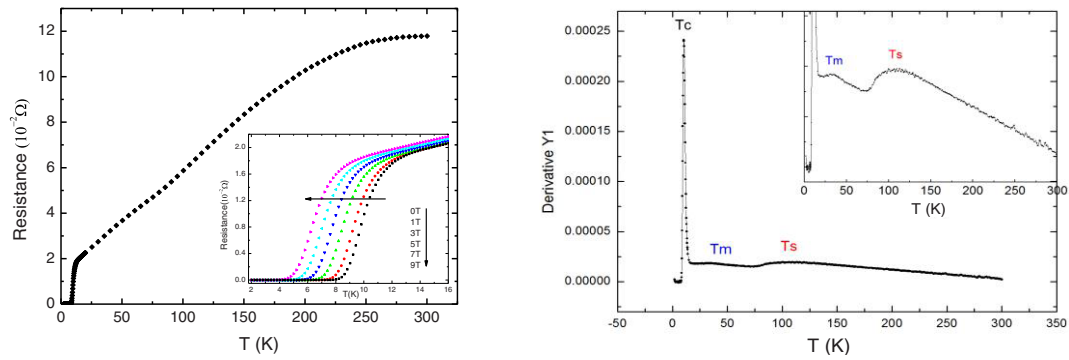


**Figure 12.** (Left) Temperature dependence of resistivity of  $\beta$ -FeSe $_{1-x}$  single crystals where the inset shows the magnetic field dependence of the resistive transition; (right) derivative  $dR/dT$  of the resistivity of  $\beta$ -FeSe $_{1-x}$  single crystal as a function of temperature. It is rescaled in the inset to reveal anomalies at  $\sim 100$  and  $\sim 40$  K.

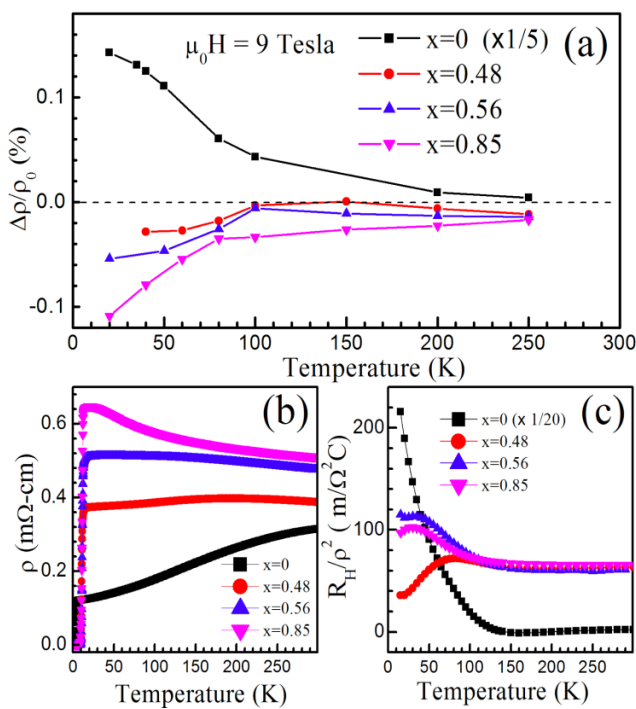


**Figure 13.** Temperature dependence of transport properties of FeSe $_{1-x}$ Te $_x$  films with  $x = 0, 0.48, 0.56$  and  $0.85$ : (a) MR, (b) resistivity and (c) Hall coefficient  $R_H/\rho^2$ .

Figure 13 shows the temperature dependences of magnetoresistance (MR), resistivity ( $\rho$ ) and Hall coefficient ( $R_H$ ) of FeSe $_{1-x}$ Te $_x$  with different Te contents. The contribution from Lorentz force dominates MR in pure FeSe films in the entire temperature range, and the negative MR term strengthens with Te substitution, as shown in figure 13(a); meanwhile, the character of the  $\rho$ - $T$  curve changes from metallic to semiconducting, figure 13(b). This evolution implies a significant increase of impurity scattering rate of the carriers in highly Te-substituted samples. The weak-localization effect is non-negligible in dirty metals, which results in a weakly semiconductor-like temperature dependence of resistivity and in the negative MR. It is well known that the value  $k_F l$  is a measure of weak-localization effect, where  $k_F$  is the Fermi wave factor and  $l$  is the

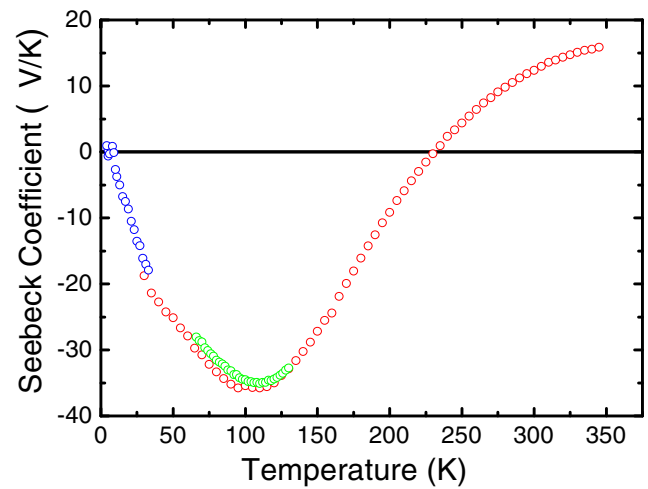


**Figure 14.** Temperature dependence of Seebeck coefficient of single-crystal  $\beta$ -FeSe $_{1-x}$ .

mean free path of carriers. The values of  $l$  and  $v_F$  can be estimated from the resistivity and Hall coefficient at room temperature using the Drude model;  $k_F l$  is approximately 5.8 for  $x = 0.85$ , which indicates a non-negligible contribution of the weak-localization effect in resistivity. In addition, the magnitude of MR increases around 100 K, for both pure FeSe and highly Te-substituted samples. This rise coincides with the structural distortion of FeSe superconductor. This significant change is also observed in the Hall coefficient, as shown in figure 13(c), which shows a sharp rise in the Hall coefficient at  $\sim 140$  K. This phenomenon could result from the change of carrier scattering rate that may be associated with the structural distortion.

In addition to the observed resistivity anomaly at  $\sim 100$  K associated with the structural distortion, the low-temperature thermoelectric power of  $\beta$ -FeSe $_{1-x}$ , shown in figure 14, also exhibits a minimum at the temperature where the structural distortion appears. Another interesting feature is the crossover from positive to negative value around 230 K, which is discussed below. Such an anomaly in thermoelectric power is not unique for  $\beta$ -FeSe $_{1-x}$  and was observed in other Fe-based superconductors.

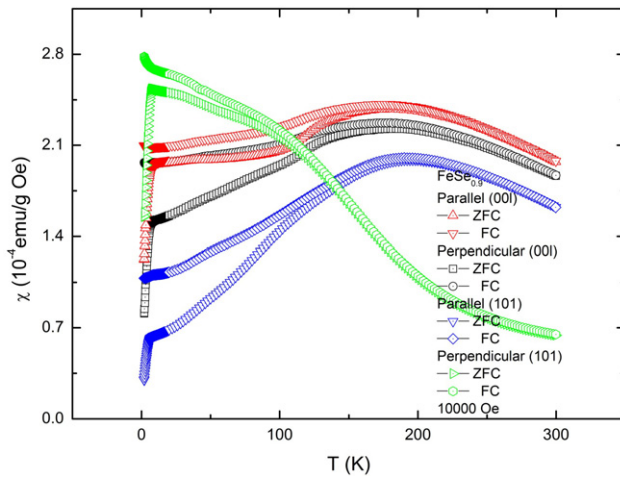


**Figure 15.** Magnetic susceptibility  $\chi$  versus temperature of the FeSe crystals measured with H (30 Oe—red and black; 10 000 Oe—blue and green) parallel to (001)—red; perpendicular to (001)—black; parallel to (101)—blue, and perpendicular to (101)—green.

### 5.3. Magnetic properties

The availability of large plate-like crystals allowed us to measure the orientation dependence of the magnetic susceptibility of  $\beta$ -FeSe $_{1-x}$ . Figure 15 shows the temperature dependences of the susceptibility with the applied field parallel or perpendicular to the (101) axis. The observed strong anisotropy suggests that the charges along (101) may behave more like free electrons, whereas those perpendicular to the (101) axis are more localized. An additional anomaly exists showing the separation between the zero-field cooling and field cooling data at  $\sim 200$  K. The origin of this strong anisotropy is not well understood. One possible hint is the presence of orbital modification at this temperature.

## 6. Summary of experimental observations

We can summarize the observed features as follows:

1. At temperatures close to 200 K the magnetic susceptibility of superconducting  $\beta$ -FeSe $_{1-x}$  exhibits anomalous behavior so that the field-cooling data differ from the zero-field cooling curves and there is a strong anisotropy when the magnetic field is directed along or perpendicular to the (101) axis. These features are attributed to the orbital modification due to the hybridization of the Fe d and Se p orbitals.
2. An anomaly also appears at around 150 K that corresponds to a rapid increase in the Hall coefficient on cooling. It suggests that the change in the density of states near the Fermi level results from the orbital modification.
3. Several features appear in the electrical resistivity on cooling before the onset of superconductivity, such as a broad hump at  $\sim 200$  K, a slight dip at  $\sim 100$  K and a drop at  $\sim 40$  K. The high-temperature hump is not well understood, but is likely related to the magnetic susceptibility anomaly mentioned above. The anomaly at 100 K is associated with the structural distortion,

which was confirmed by x-ray and neutron diffraction experiments.

4. Substitution of Fe in  $\beta$ -FeSe $_{1-x}$  with transition metal elements demonstrated that superconductivity is suppressed by non-magnetic element such as Cu, but is less affected by magnetic ions like Mn. Detailed structure analysis of the non-superconducting samples show that superconductivity is closely correlated with the low-temperature structural distortion. This conclusion is confirmed by studies on  $\beta$ -FeSe $_{1-x}$  thin films and by a detailed chemical stoichiometry investigation by McQueen *et al* [48].
5. Thermoelectric power exhibits an anomaly in  $\beta$ -FeSe $_{1-x}$  at the temperature where structural distortion occurs, suggesting that the structure distortion affects the band structure.
6. Local probe experiments including nuclear magnetic resonance and muon spin resonance show a strong spin fluctuation, which can also be associated with the structural distortion.
7. The superconducting transition temperature of  $\beta$ -FeSe $_{1-x}$  can be enhanced up to about 40 K by the application of pressure. It is thus interesting to identify the origin of the resistivity anomaly appearing at  $\sim 40$  K.

The features summarized above are pertinent to the origin of superconductivity in  $\beta$ -FeSe $_{1-x}$  and may also apply to other Fe-based superconductors. It was suggested that in the Fe-based superconductors electron pairing is likely mediated by spin fluctuations [49, 50] and is likely entangled in the electronic nematic order (a rotational symmetry-breaking phase) [51–54]. Both nematicity and magnetic fluctuations are generally associated with the structural distortion at high temperatures. The interplay among different degrees of freedom is thus the core of diverse questions involving Fe-based superconductors. Ongoing debates discuss how the nematicity develops and whether it induces precursory electron condensations [55].

## 7. Structure—properties correlation and superconductivity in $\beta$ -FeSe

Recent photoemission spectroscopic studies [51] indicated that breaking of the electronic symmetry is induced by unbalanced populations in Fe  $3d_{xz}$  and  $3d_{yz}$  orbitals, driven by the orbital splitting near the structural transition temperature ( $T_s$ ). This effect causes changes in transport properties through a Fermi surface reconstruction [55] and redistributions of the optical spectral weight with photon energies up to the visible range [53, 54]. Even with these efforts, no generally accepted picture has emerged due to limited observations on the orbital modification at temperatures across  $T_s$  [51]. It thus remains unclear which role nematicity plays in relation to the lattice symmetry breaking and high- $T_c$  superconductivity.

To gain more insight into the correlation between superconductivity and the low-temperature structural

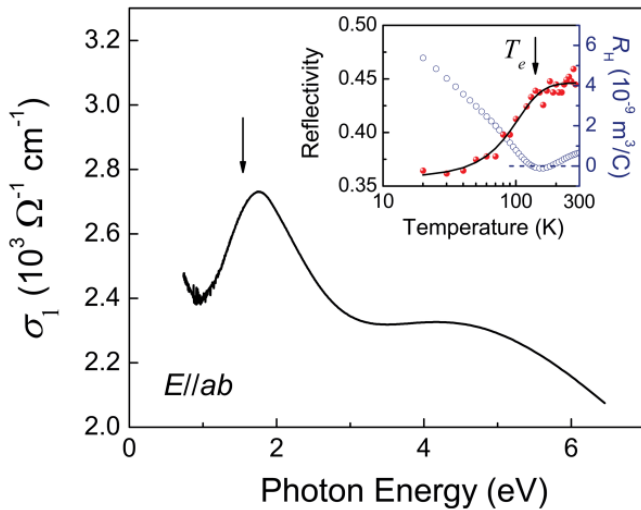


**Figure 16.** Real part of the optical conductivity  $s(w) = is_1(w) + is_2(w)$ . The arrow indicates the photon energy (1.55 eV) adopted in the steady-state and transient reflectivity experiments. The inset shows the temperature dependences of optical reflectivity (solid dots) and Hall coefficient  $R_H$  (open dots); the solid line guides the eye [56].

distortion, we carried out time-resolved optical studies of electron and phonon dynamics [56–59], which can clarify the changes of the band structure near the Fermi level  $E_F$  and underlying interatomic interactions. The major contribution to the optical response of FeSe in the visible spectral range comes from intraband Fe d and interband Fe d to hybridized Fe-d/Se-p transitions [60]. Figure 16 shows the real part of the optical conductivity  $s_1(w)$  derived from room-temperature ellipsometric measurements. The distinct peak at  $\sim 1.8$  eV is associated with the transition from Fe d to Fe-d/Se-p hybridized orbitals and the two major peaks of the density of states near  $E_F$  [60]. To look into the temperature-dependent orbital change, we used near-infrared photons (1.55 eV, an arrow in figure 16) that resonantly probe this interband transition. The inset of figure 16 shows the corresponding temperature-dependent optical reflectivity, where a clear reduction can be found at  $T < 130 \pm 10$  K (the marker  $T_e$  is set at 140 K). This feature indicates a redistribution of the optical spectral weight and the orbital modification at low temperatures.

Figure 17(a) shows the evolution of reflectivity in the picosecond scale at different temperatures. The high-temperature traces can be well described by a single relaxation, whereas an additional sub-ps relaxation is observed at low temperatures. We modeled the picosecond response by the equation  $\Delta R/R = A_{\text{fast}} \exp(-t/\tau_{\text{fast}}) + A_{\text{slow}} \times \exp(-t/\tau_{\text{slow}}) + A_{\text{step}}$ , where  $A_{\text{step}}$  represents the sub-ns recovery.

Figure 17(b) shows the temperature-dependent fitting variables derived from the data in figure 17(a). From the inset of figure 17(b), the sub-ps relaxation (fast one) is found to emerge below 130–140 K, and its magnitude  $A_{\text{fast}}$  gradually increases with decreasing temperature until  $\sim 70$  K. This feature allows us to attribute this signal to the gap-like quasiparticles, which can be phenomenologically explained in

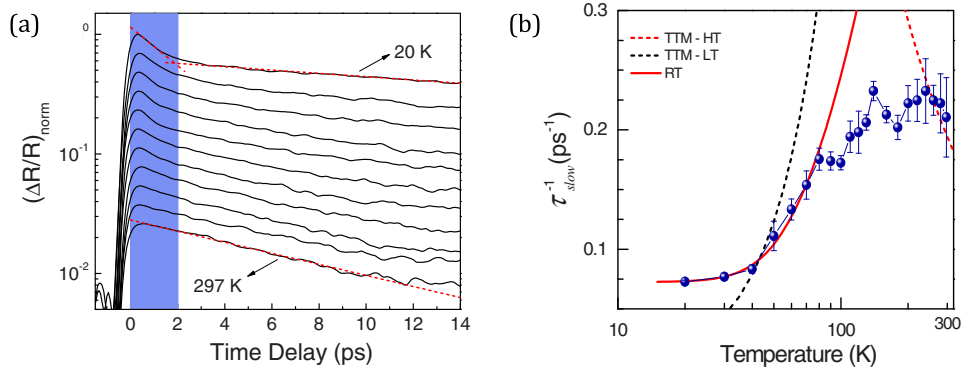
the framework of Rothwarf–Taylor (RT) theory [61]—in the presence of a gap near  $E_F$ , hot carriers will accumulate in the quasiparticle state above the gap and wait for recombination via scatterings with high-energy phonons. The bottleneck model by Demsar *et al* [57] and Mertelj *et al* [58] provides an analytical description of the experimental data, enabling a preliminary estimation of the effective gap at  $\Delta = 36 \pm 4$  meV.

The picosecond relaxation also contains a contribution from carrier–phonon (c–p) thermalization that is ubiquitous at all temperatures and reflects the c–p coupling strength [58, 59]. Intriguingly, we find that the measured c–p thermalization rate strongly depends on the film orientation, indicating the anisotropy of the probe transition matrix element. For a probe polarization parallel to the *ab* plane, the c–p thermalization rate is  $2.7 \text{ ps}^{-1}$ , which agrees with the theoretical prediction ( $3.5 \text{ ps}^{-1}$ ). This striking contrast reveals a dramatic change in the contribution of bands with non-vanishing interplane wavevectors to  $\Delta R/R$  and considerable mass of the carriers therein<sup>4</sup>. This anisotropic c–p coupling may help understand the distinctive interplane optical conductivity and resistivity of Fe-based superconductors [63, 64].

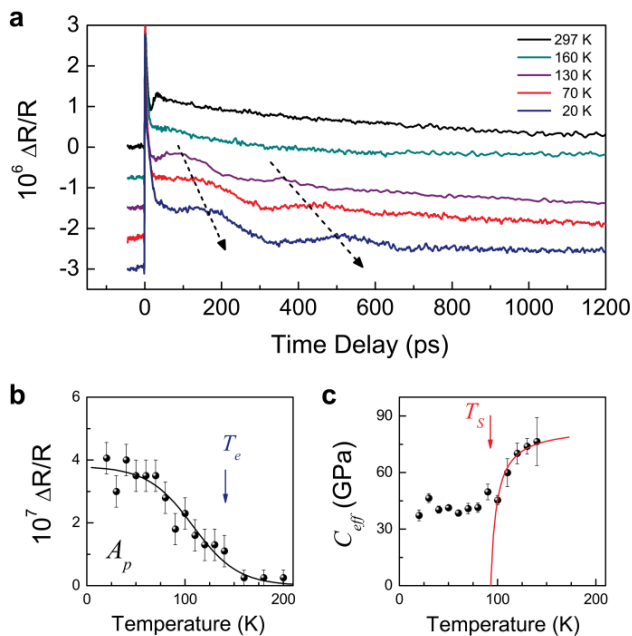
The temperature-dependent c–p thermalization is further analyzed with the two-temperature model (TTM), which provides the commonly accepted descriptions in metals [65], and the fitting results are shown in figure 17(b). Obviously, the TTM predicts an overestimated temperature dependency of  $\tau_{\text{slow}}^{-1} (\propto T^2 \sim T^3)$  at low temperatures, where the gap could participate in the carrier relaxation. To alleviate this deviation, a model including a gap near  $E_F$  is adopted. The modified c–p relaxation time [66], obtained by analytically solving the RT theory, led to an effective energy gap of  $\Delta = 9.2 \pm 1.5$  meV, where a satisfactory description of the low-temperature experiment supports the existence of an energy gap. The same order of magnitude of the gap width revealed from the fast and slow relaxations in  $\beta$ -FeSe<sub>1-x</sub> (36 and 9.2 meV) quantitatively support the unified scenario of the gap formation at high temperatures ( $T > T_c$ ). The onset of the gap opening can be set at  $\sim 140$  K, where the emergence of gap-like quasiparticles (130–140 K), a small singularity of  $\tau_{\text{slow}}^{-1}$  ( $140 \pm 5$  K), and dramatic changes in transport properties ( $140 \pm 10$  K) are observed.

Figure 18(a) shows the transient optical reflectivity on the sub-nanosecond timescale. Here our concern is the oscillatory feature emerging below 140–150 K. It becomes more distinct and has a lower oscillation frequency (3–4.2 GHz,  $\hbar\omega \sim 0.01$  meV) at lower temperatures. Analysis of this feature is performed by fitting with a damped sinusoidal function  $A_p \exp(-t/\tau_p) \sin(\omega t + f)$ . This signal can be attributed to the round-trip propagation of photoexcited coherent acoustic phonons, i.e. macroscopic film vibrations. It periodically modulates the thickness of the FeSe film with  $w = pV_g/L$  and can reveal the effective longitudinal stiffness  $C_{\text{eff}} \equiv rV_p^2$  (figure 18(c)), where  $L$  is film thickness,  $r$  is mass density, and  $V_g$  and  $V_p$  are group and phase velocities

<sup>4</sup> Large mass causes inefficient energy exchange with phonons and with the carriers in other bands. See, for example, [62].



**Figure 17.** (a) Picosecond response of transient optical reflectivity  $\Delta R/R$  measured at different temperatures (solid lines from top to bottom: 20, 40, 60, 80, 100, 120, 140, 180, 220, 260 and 297 K). The data are normalized and vertically shifted for clarity. The dotted lines depict relaxation processes. (b) Temperature dependences of  $\tau_{\text{slow}}^{-1}$  and  $A_{\text{fast}}$  (dots). The dotted lines are TTM predictions for poor metals in the high-temperature and low-temperature limits (HT and LT) with the same c-p coupling constant  $\lambda$ . The solid line is the Rothwarf-Taylor (RT) fit.



**Figure 18.** (a) Transient optical reflectivity changes measured at different temperatures (solid lines). The spectra are vertically shifted for clarity. The dashed lines indicate the decrease of the oscillation frequency with decreasing temperature. Temperature dependences of the oscillation amplitude  $A_p$  (b) and effective stiffness (c). The fitting curve is based on the formula  $C_{\text{eff}} = C_{\text{eff}}^0(T - \Theta)/(T - T_s)$  [68], where  $C_{\text{eff}}^0$  is the high-temperature effective stiffness and  $\Theta$  is a fitting parameter [56].

of the quasi-longitudinal waves along the [101] direction, respectively [66]. This interpretation of coherent phonon detection is supported by the agreement between the measured  $C_{\text{eff}}$  at the highest temperature ( $76 \pm 12$  GPa at 140 K) and the available literature value ( $77$  GPa at room temperature)<sup>5</sup>.

The finding above provides valuable clues to both electronic and elastic properties. On cooling, FeSe first

<sup>5</sup>  $\rho = 5.65$  g cm $^{-3}$ ; the walk-off angle of the quasi-longitudinal wave ( $\sim 16^\circ$ ) was assumed to be temperature independent.

exhibits a significant suppression of the optical absorption below 140 K (figure 18(b)), consistent with the distinct spectral weight transfer, as well as orbital modifications, below  $\sim T_e$  (inset of figure 16). Second, the  $C_{\text{eff}}$  exhibits a temperature-dependent reduction above 90 K and remains nearly constant at lower temperatures. The phonon softening originates from the lattice instability above the structural transition and is arrested at  $T_s$ , as previously observed by ultrasonic techniques [67, 68]. The coherent phonon dynamics indicates a transition temperature  $T_s$  of  $90 \pm 3$  K (figure 18(c)), consistent with the x-ray studies on nearly stoichiometric  $\beta$ -FeSe $_{1-x}$  [7, 48] and remarkably lower by  $\sim 50$  K than the onset of the electronic modification ( $T_e$ ).

From the fact of  $T_e > T_s$ , we propose that short-range orders evolve into long-range ones and induce the lattice symmetry breaking at  $T_s$ . As mentioned above, the nematicity picture is consistent with dramatic changes in the Hall coefficient  $R_H$  and the Seebeck coefficient  $S$  [69]. The key point is the striking coincidence of the onset of changes in the transport properties ( $140 \pm 10$  K) with  $T_e$ , supporting the scenario that the short-range nematic charge and/or orbital orders induce Fermi surface reconstruction and gap opening above the structural transition.

The carrier dynamics study has relevant implications for the high-temperature anomalies of Fe-based superconductors. Our data and the systematic studies of the structural effect on the cooperation/competition of spin-fluctuation modes and superconductivity [48, 70] suggest that the structural transition is not only driven by the orbital order, but also strongly interacts with it in this correlated system. The observations on the optical spectral weight transfer and opening of the high-temperature gap, as well as alterations in the transport properties, reflect the nature of the short-range charge and/or orbital orders that cause the Fermi surface reconstruction and the gap opening. These *in situ* and stress-free studies, therefore, not only provide the first evidence for short-range orders *above* the structural phase transition, but also support the picture that nematicity plays an important role in the precursor state of high- $T_c$  superconductors.

## 8. Conclusions

We have summarized the methods of growing high-quality single crystals and oriented thin films with controllable orientation. The available high-quality samples provide researchers with opportunities to characterize the physical properties in more details, which are critical for understanding the mechanism of superconductivity. The results of magnetic, electrical and thermo-transport measurements indicate an orbital modification at around 140–200 K that leads to the structural distortion at  $\sim 100$  K. There is also strong evidence for the presence of spin fluctuation at the structure distortion temperature. More direct evidence to support this speculation came from recent results on quasiparticle and acoustic phonon dynamics. Our observations suggest the opening of an energy gap (in the order of  $\sim 36$  meV) below 130–140 K, which is accompanied by a coincident transfer of optical spectral weight in the visible range and alterations in the transport properties. These observations provide compelling evidence that the modification of the electronic structure occurs *prior* to the lattice transformation. They further suggest that the high-temperature gap and the lattice symmetry breaking are driven by short-range orbital and/or charge orders, implying a close correlation between nematicity and the precursor phase.

## Acknowledgments

The authors thank all their colleagues, including F C Hsu, J Y Luo, H H Chang, T W Huang, T K Chen, C C Chang, C L Chen, Y C Wen and many others for their critical contributions. We also thank Professors T K Lee, C C Chi and Y Y Chen for their valuable suggestions. The authors acknowledge financial support from the Academia Sinica and the National Science Council of Taiwan.

## References

- [1] Hsu F C *et al* 2008 *Proc. Natl Acad. Sci. USA* **105** 14262
- [2] Mizuguchi Y *et al* 2008 *Appl. Phys. Lett.* **93** 152505
- [3] Yeh K W *et al* 2008 *Europhys. Lett.* **84** 37002
- [4] Wu M K *et al* 2009 *Physica C* **469** 340
- [5] Mok B H *et al* 2009 *Cryst. Growth Des.* **9** 3260
- [6] Guo J, Jin S, Wang G, Wang S, Zhu K, Zhou T, He M and Chen X 2010 *Phys. Rev. B* **82** 180520
- [7] Wang M J, Luo J Y, Huang T W, Chang H H, Chen T K, Hsu F C, Wu C T, Wu P M, Chang A M and Wu M K 2009 *Phys. Rev. Lett.* **103** 117002
- [8] Huang S X, Chien C L, Thampy V and Broholm C 2010 *Phys. Rev. Lett.* **104** 217002
- [9] Okamoto H 1991 *J. Phase Equilib.* **12** 383
- [10] Zhang S B *et al* 2009 *Supercond. Sci. Technol.* **22** 015020
- [11] Patel U, Hua J, Yu S H, Avci S, Xiao Z L, Claus H, Schlueter J, Vlasko-Vlasov V V, Welp U and Kwok W K 2009 *Appl. Phys. Lett.* **94** 082508
- [12] Karkin A E, Titov A N, Galieva E G, Titov A A and Goshchitskii B N 2010 arXiv:0911.1194
- [13] Zhigadlo N D, Katrych S, Bukowski Z, Weyeneth S, Puzniak R and Karpinski J 2008 *J. Phys.: Condens. Matter* **20** 342202
- [14] Karpinski J, Zhigadlo N D, Katrych S, Puzniak R, Rogacki K and Gonnelli R 2007 *Physica C* **456** 3
- [15] Lee C H, Kito H, Ihara H, Akita K, Yanase N, Sekine C and Shirota I 2004 *J. Cryst. Growth* **263** 358
- [16] Ge J Y, Cao S J, Yuan S J, Kang B J and Zhang J C 2010 *J. Appl. Phys.* **108** 053903
- [17] Sales B C, Sefat A S, McGuire M A, Jin R Y, Mandrus D and Mozharivskij Y 2009 *Phys. Rev. B* **79** 094521
- [18] Chen G F, Chen Z G, Dong J, Hu W Z, Li G, Zhang X D, Zheng P, Lu J L and Wang N L 2009 *Phys. Rev. B* **79** 140509
- [19] Noji T, Suzuki T, Abe H, Adachi T, Kato M and Koike Y 2010 *J. Phys. Soc. Japan* **79** 084711
- [20] Tsurkan V, Deisenhofer J, Günther A, Kant Ch, Klemm M, Krug von Nidda H A, Schrettle F and Loidl A 2011 *Europhys. J. B* **79** 289
- [21] Yeh K W, Ke C T, Huang T W, Chen T K, Huang Y L, Wu P M and Wu M K 2009 *Cryst. Growth Des.* **9** 4847
- [22] Thomas E L, Wong-Ng W, Phelan D and Millican J N 2009 *J. Appl. Phys.* **105** 073906
- [23] Mizuguchi Y, Tomioka F, Tsuda S, Yamaguchi T and Takano Y 2009 *J. Phys. Soc. Japan* **78** 074712
- [24] Zhang S B, Lei H C, Zhu X D, Li G, Wang B S, Li L J, Zhu X B, Song W H, Yang Z R and Sun Y P 2009 *Physica C* **469** 1958
- [25] Williams J, McQueen T M, Ksenofontov V, Felser C and Cava R J 2009 *J. Phys.: Condens. Matter* **21** 305701
- [26] Huang T W *et al* 2010 *Phys. Rev. B* **82** 104502
- [27] Günther A, Deisenhofer J, Kant Ch, Krug von Nidda H A, Tsurkan V and Loidl A 2011 *Supercond. Sci. Technol.* **24** 045009
- [28] Zhang A M, Xia T L, Kong L R, Xiao J H and Zhang Q M 2010 *J. Phys.: Condens. Matter* **22** 245701
- [29] Shipra R, Takeya H, Hirata K and Sundaresan A 2010 *Physica C* **470** 528
- [30] Gawryluk D J, Fink-Finowicki J, Wisniewski A, Puzniak R, Domukhovski V, Diduszko R, Kozłowski M and Berkowski M 2010 arXiv:1010.4217
- [31] Wang A F *et al* 2011 *Phys. Rev. B* **83** 060512
- [32] Krzton-Maziopa A, Shermadini Z, Pomjakushina E, Pomjakushin V, Bendele M, Amato A, Khasanov R, Luetkens H and Conder K 2011 *J. Phys.: Condens. Matter* **23** 052203
- [33] Pomjakushina E, Conder K, Pomjakushin V, Bendele M and Khasanov R 2009 *Phys. Rev. B* **80** 024517
- [34] Mizuguchi Y, Hara Y, Deguchi K, Tsuda S, Yamaguchi T, Takedam K, Kotegawa H, Tou H and Takano Y 2010 *Supercond. Sci. Technol.* **23** 054013
- [35] Yuan H Q, Singleton J, Balakirev F F, Baily S A, Chen G F, Luo J L and Wang N L 2009 *Nature* **457** 565
- [36] Lee K W, Pardo V and Pickett W E 2008 *Phys. Rev. B* **78** 174502
- [37] Medvedev S *et al* 2009 *Nature Mater.* **8** 630
- [38] Bendele M, Babkevich P, Katrych S, Gvasaliya S N, Pomjakushina E, Conder K, Roessli B, Boothroyd A T, Khasanov and Keller H 2010 *Phys. Rev. B* **82** 212504
- [39] Sun L L, Chen X J, Guo J, Gao P W, Huang Q Z, Chen H X L, Chen G F and Wu Q 2012 *Nature* **483** 67
- [40] Chen T K, Ke C T, Chang H H, Huang T W, Yeh K W, Chang C C, Hsu P C, Wu C T and Wang M J 2010 *Thin Solid Films* **519** 1540
- [41] Nie Y F, Brahimi E, Budnick J I, Hines W A, Jain M and Wells B O 2009 *Appl. Phys. Lett.* **94** 242505
- [42] Han Y, Li W Y, Cao L X, Zhang S, Xu B and Zhao B R 2009 *J. Phys.: Condens. Matter* **21** 235702
- [43] Jourdan M and ten Haaf S 2010 *J. Appl. Phys.* **108** 023913
- [44] Agatsuma S, Yamagishi T, Takeda S and Naito M 2010 *Physica C* **470** 1468
- [45] Li L, Yang Z R, Sun Y P, Zhang J Y, Shen D Z and Zhang Y H 2011 *Supercond. Sci. Technol.* **24** 015010
- [46] Bellingeri E, Pallecchi I, Buzio R, Gerbi A, Marrè D, Cimberle M R, Tropeano M, Putti M, Palenzona A and Ferdeghini C 2010 *Appl. Phys. Lett.* **96** 102512

- [47] Han Y, Li W Y, Cao L X, Wang X Y, Xu B, Zhao B R, Guo Y Q and Yang J L 2010 *Phys. Rev. Lett.* **104** 017003
- [48] McQueen T M, Williams A J, Stephens P W, Tao J, Zhu Y, Ksenofontov V, Casper F, Felser C and Cava R J 2009 *Phys. Rev. Lett.* **103** 057002
- [49] Stewart G R 2011 *Rev. Mod. Phys.* **83** 1589
- [50] Imai I, Ahilan K, Ning F L, McQueen T M and Cava R J 2009 *Phys. Rev. Lett.* **102** 177005
- [51] Fisher I R, Degiorgi L and Shen Z X 2011 *Rep. Prog. Phys.* **74** 124506
- [52] Chu J H, Analytis J G, De Greve K, McMahon P L, Islam Z, Yamamoto Y and Fisher I R 2010 *Science* **329** 824
- [53] Nakajima M *et al* 2011 *Proc. Natl Acad. Sci. USA* **108** 12238
- [54] Charnukha A, Popovich P, Matiks Y, Sun D L, Lin C T, Yaresko A N, Keimer B and Boris A V 2011 *Nature Commun.* **2** 219
- [55] See, for example, Daou R *et al* 2010 *Nature* **463** 519
- [56] Wen Y C, Wang K J, Chang H H, Luo J Y, Shen C C, Liu H L, Sun C K, Wang M J and Wu M K 2012 *Phys. Rev. Lett.* **108** 267002
- [57] Demsar J, Podobnik B, Kabanov V V, Wolf Th and Mihailovic D 1999 *Phys. Rev. Lett.* **82** 4918
- [58] Mertelj T, Kabanov V V, Gadermaier C, Zhigadlo N D, Katrych S, Karpinski J and Mihailovic D 2009 *Phys. Rev. Lett.* **102** 117002
- [59] Chia E E M *et al* 2010 *Phys. Rev. Lett.* **104** 027003
- [60] Subedi A, Zhang L J, Singh D J and Du M H 2008 *Phys. Rev. B* **78** 134514
- [61] Rothwarf A and Taylor B N 1967 *Phys. Rev. Lett.* **19** 27
- [62] Demsar J, Averitt R D, Ahn K H, Graf M J, Trugman S A, Kabanov V V, Sarrao J L and Taylor A J 2003 *Phys. Rev. Lett.* **91** 027401
- [63] Moon S J, Homes C C, Akrap A, Xu Z J, Wen J S, Lin Z W, Li Q, Gu G D and Basov D N 2011 *Phys. Rev. Lett.* **106** 217001
- [64] Chen G F, Li Z, Dong J, Li G, Hu W Z, Zhang X D, Song X H, Zheng P, Wang N L and Luo J L 2008 *Phys. Rev. B* **78** 224512
- [65] Kabanov V V and Alexandrov A S 2008 *Phys. Rev. B* **78** 174514
- [66] Talbayev D *et al* 2010 *Phys. Rev. Lett.* **104** 227002
- [67] Chandra S and Islam A K M A 2010 *Physica C* **470** 2072
- [68] Fernandes R M, VanBebber L H, Bhattacharya S, Chandra P, Keppens V, Mandrus D, McGuire M A, Sales B C, Sefat A S and Schmalian J 2010 *Phys. Rev. Lett.* **105** 157003
- [69] Lüthi B and Millican J N 2009 *J. Appl. Phys.* **105** 073906  
Wu M-K in preparation
- [70] Moon C Y and Choi H J 2010 *Phys. Rev. Lett.* **104** 057003